Simulating quantum spin models using Rydberg-excited atomic ensembles in magnetic microtrap arrays

OPEN ACCESS
IOP Publishing
Journal of Physics B: Atomic, Molecular and Optical Physics
J. Phys. B: At. Mol. Opt. Phys. **50** (2017) 074001 (13pp)
https://doi.org/10.1088/1361-6455/aa6149

Simulating quantum spin models using Rydberg-excited atomic ensembles in magnetic microtrap arrays

Shannon Whitlock[1,2,8], **Alexander W Glaetzle**[3,4,5,6] **and Peter Hannaford**[7]

[1] Physikalisches Institut, Universität Heidelberg, Im Neuenheimer Feld 226, D-69120 Heidelberg, Germany
[2] IPCMS (UMR 7504) and ISIS (UMR 7006), Université de Strasbourg and CNRS, 67000 Strasbourg, France
[3] Institute for Quantum Optics and Quantum Information of the Austrian Academy of Sciences, A-6020 Innsbruck, Austria
[4] Institute for Theoretical Physics, University of Innsbruck, A-6020 Innsbruck, Austria
[5] Centre for Quantum Technologies, National University of Singapore, 3 Science Drive 2, Singapore
[6] Clarendon Laboratory, University of Oxford, Parks Road, Oxford OX1 3PU, United Kingdom
[7] Centre for Quantum and Optical Science, Swinburne University of Technology, Melbourne, Victoria 3122, Australia

E-mail: whitlock@ipcms.unistra.fr and phannaford@swin.edu.au

Received 31 July 2016, revised 19 October 2016
Accepted for publication 3 November 2016
Published 10 March 2017

Abstract

We propose a scheme to simulate lattice spin models based on strong, long-range interacting Rydberg atoms stored in a large-spacing array of magnetic microtraps. Each spin is encoded in a collective spin state involving a single nS or $(n + 1)S$ Rydberg atom excited from an ensemble of ground-state alkali atoms prepared via Rydberg blockade. After the excitation laser is switched off, the Rydberg spin states on neighbouring lattice sites interact via general XXZ spin–spin interactions. To read out the collective spin states we propose a single Rydberg atom triggered avalanche scheme in which the presence of a single Rydberg atom conditionally transfers a large number of ground-state atoms in the trap to an untrapped state which can be readily detected by site-resolved absorption imaging. Such a quantum simulator should allow the study of quantum spin systems in almost arbitrary one-dimensional and two-dimensional configurations. This paves the way towards engineering exotic spin models, such as spin models based on triangular-symmetry lattices which can give rise to frustrated-spin magnetism.

Keywords: spin-models, Rydberg interactions, magnetism, microtrap arrays, atomic ensembles, quantum simulation

(Some figures may appear in colour only in the online journal)

1. Introduction

Periodic arrays of quantum spins coupled through magnetic interactions represent an archetypal model system in quantum many-body physics, non-equilibrium physics, statistical physics and condensed matter physics, with potential implications ranging from quantum magnetism to quantum information science, spintronics and high-temperature superconductivity [1–3]. Apart from a few special cases, such models are generally computationally intractable due to extreme complexity

[8] Author to whom any correspondence should be addressed.

arising from quantum entanglement between the spins. Furthermore, experimental studies on solid-state spin systems are often restricted by uncontrolled disorder and random couplings to the environment as well as limited control over system parameters.

There is currently a growing interest in utilising ultracold atoms stored in periodic lattices to simulate many-body and condensed matter systems (e.g., [2–8]). Ultracold atoms trapped in periodic lattices can allow precise control over system parameters, such as the inter-particle interaction, lattice geometry and disorder, and, in principle, provide an ideal platform to achieve almost perfect realisations of a variety of lattice spin models [2–8]. Most proposals to date have been based on tunnelling and on-site interactions in optical lattices, in which the magnetic interaction energy scales are set by a superexchange interaction whose strength scales as $J \sim t^2/U$ [2] (with t the tunnelling rate and U the on-site interaction energy). The t^2-dependence results in extremely small magnetic energy scales, of the order of only a few tens of hertz, corresponding to just a few nanokelvin. Thus, with spin models based on tunnelling dynamics, a major experimental challenge is the requirement of extremely low temperatures, close to or beyond the limits of current state-of-the-art atom cooling techniques [6, 9]. Possible ways to circumvent this very low-temperature requirement have been proposed, including the use of ultracold polar molecules [10] and Rydberg-dressed ground-state atoms [7, 11] featuring widely tunable long-range interactions which can be effective over distances much larger than typical optical lattice periods.

In this paper we propose the use of long-range interacting Rydberg atoms prepared in a large-spacing (several μm) lattice of magnetic microtraps [12–18] to simulate lattice spin models. This scheme is similar to earlier proposals to create Rydberg quantum gates in mesoscopic ensembles in the context of quantum information science [19–22]. Each spin is encoded in a collective spin state involving a single rubidium $n_\downarrow S$ or $n_\uparrow S$ Rydberg atom in an ensemble of ground-state Rb atoms prepared via Rydberg blockade [23] (figure 1). The use of atomic ensembles avoids the problem of exact single-atom filling of lattice sites and single-atom detection, which is a requirement for schemes based on Rydberg-dressed ground-state atoms [7, 11], and also helps greatly with the initialisation and readout of individual Rydberg spin states. The long-range and widely tunable interactions between Rydberg atoms combined with a large-spacing between the interacting spins readily facilitates site-resolved detection using standard optical imaging techniques. The use of Rydberg S-states allows for nearly isotropic XXZ-type spin–spin interactions which can extend beyond nearest-neighbours. The timescales associated with atomic motion (∼ms) or lifetimes of high nS Rydberg states (>20μs) [24] are long compared to the timescales associated with strong Rydberg–Rydberg interactions (∼1μs), which enables investigation of non-equilibrium spin dynamics on both short and long times, including, for example, the build-up of spin–spin correlations following a sudden quench of the system parameters.

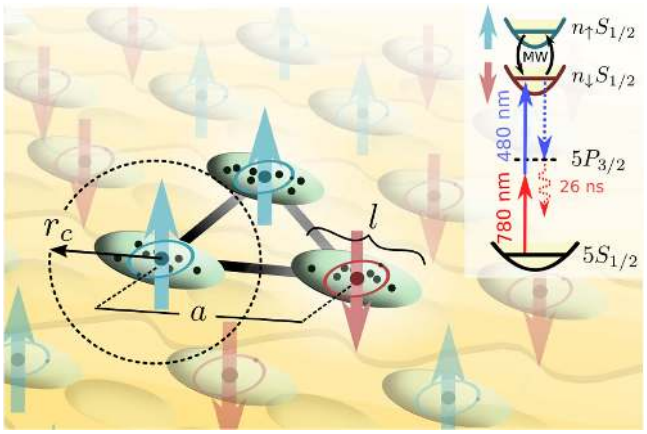

Figure 1. Proposed experimental setup for simulating quantum spin models in atomic ensembles confined in a microtrap array. Two spin states $|\downarrow\rangle$ and $|\uparrow\rangle$ are encoded in a single two-step excitation to the Rydberg state $|n_\downarrow S\rangle$ or $|n_\uparrow S\rangle$, shared amongst all atoms in an ensemble. The spatial extent of each ensemble is ℓ, the on-site blockade radius is r_c and the lattice spacing is a, with $a \gtrsim r_c \gg \ell$. The inset shows the internal level structure of a single atom with the states involved in the detection processes marked with dashed lines. General spin–spin interactions occur via long-range van der Waals interactions between the $|n_\downarrow S\rangle$ and $|n_\uparrow S\rangle$ states.

2. Simulating quantum spin models

As a concrete experimental platform we consider an array of magnetic microtraps created by patterned magnetic films on an atom chip [13–18, 25]. A general algorithm has been developed to design the required magnetic patterns, enabling microtrap arrays to be produced with nearly-arbitrary 2D symmetries and orientations of the magnetic field at the bottom of each microtrap, without restrictions imposed by optical fields [15]. Lattices of magnetic microtraps with triangular and square symmetry with a period of 10 μm have already been realised and loaded with small atomic ensembles, each consisting of a few hundred atoms [22].

For our implementation we assume each site i contains an ensemble of N_i rubidium atoms confined to a characteristic size ℓ and different sites are separated by the lattice period a, with $\ell \ll a$. We consider the following excitation, interaction and detection sequence:

2.1. Initialisation

Each lattice site is prepared with precisely one Rydberg excitation, e.g., using a two-photon laser excitation involving 780 and 480 nm wavelengths tuned to the $|g\rangle \rightarrow |R^\downarrow\rangle \equiv |n_\downarrow S_{1/2}, m_j = +1/2\rangle$ transition (figure 1, inset). Assuming Poissonian statistics with a mean number of atoms $\bar{N} = 10$ the probability to load zero atoms in a given site is $<10^{-4}$; therefore we can expect large filling factors. To restrict the system to a single excitation on each site we propose to use the Rydberg blockade effect which strongly suppresses the probability to excite more than one atom in the ensemble [23]. Disorder may be introduced to the resulting spin models, either through the presence of empty sites or the random positions of the Rydberg excitations within each cloud that

modifies the nearest neighbour spin–spin couplings. Numerical simulations of the initialisation scheme including anticipated experimental limitations on the achievable filling factors is discussed in section 3.

2.2. Interaction time

Following initialisation, the excitation laser is switched off and Rydberg excitations on neighbouring lattice sites can interact as a consequence of their giant electric dipole moments (typically several kilodebye). At large separations and away from Förster resonances, Rydberg–Rydberg interactions can be treated perturbatively leading to van der Waals (vdW) interactions which scale as n^{11} [23], with n the principal quantum number. We identify two collective spin states for a single site

$$|\uparrow\rangle = \frac{1}{\sqrt{N}}\sum_j |g_1,\ldots,g_{j-1},R_j^{\uparrow},g_{j+1},\ldots,g_N\rangle,$$
$$|\downarrow\rangle = \frac{1}{\sqrt{N}}\sum_j |g_1,\ldots,g_{j-1},R_j^{\downarrow},g_{j+1},\ldots,g_N\rangle, \quad (1)$$

(see figure 1), where $|R^{\uparrow}\rangle$ ($|R^{\downarrow}\rangle$) denotes the $|n_{\uparrow}S_{1/2}, m_j = +1/2\rangle$ ($|n_{\downarrow}S_{1/2}, m_j = +1/2\rangle$) Rydberg state. These collective spin states are coherent superpositions with the single Rydberg excitation shared amongst all atoms in the ensemble [23]. This configuration will allow complex spin–spin interactions including XXZ-type spin–spin interactions as described in section 4. Additionally, the two collective spin states can be coupled using microwave frequency transitions to realise single spin rotations which simulate transverse and longitudinal magnetic fields.

2.3. Readout

To read out the collective spin state one needs to be able to detect the presence of a single Rydberg atom in a given spin state in the atomic ensemble with high fidelity. Here, the use of atomic ensembles is a significant advantage. We propose to use a single-Rydberg atom triggered ionisation 'avalanche' scheme, similar to recent observations [26–28], in which the presence of the single Rydberg atom conditionally transfers a large number of ground-state atoms in the trap to an untrapped state which can then be detected by standard site-resolved absorption imaging, as described in section 5.

In the following we identify some general criteria for this system to be suitable for the quantum simulation of spin models. First, the typical rate associated with spin–spin interactions between neighbouring sites must greatly exceed the decoherence rate predominantly given by the Rydberg state decay rate Γ. Second, to prevent interference between neighbouring sites during the initialisation phase we additionally require that the Rydberg excitation bandwidth $\sqrt{\bar{N}}\Omega$ exceeds the spin–spin interaction strength between neighbouring ensembles. Finally, we require that the interactions between atoms within each ensemble far exceed the excitation bandwidth to ensure good conditions for the Rydberg blockade. Combining these constraints we can define the following criteria:

$$\frac{|C_6|}{\ell^6} \gg \sqrt{\bar{N}}\Omega \gg \frac{|C_6|}{a^6} \gg \Gamma. \quad (2)$$

These citeria can be met for typical conditions in a large-spacing magnetic lattice [17]. To illustrate this we take the $|33S_{1/2}\rangle$ state of ^{87}Rb and assume a lattice with a period $a \approx 2.5\ \mu$m, trap size $\ell \approx 2\sigma = 0.8\ \mu$m and mean number of atoms $\bar{N} = 10$. The Rydberg state decay rate, including decay by spontaneous emission and blackbody radiation at $T = 300$ K, is $\Gamma = 2\pi \times (7.3\ \text{kHz})$ [24]. This is much smaller than the spin–spin coupling between neighbouring states $C_6/a^6 \approx 2\pi \times (0.36\ \text{MHz})$. The experimentally achievable effective two-photon Rabi frequency with collective enhancement using commercially available laser sources is typically $\sqrt{\bar{N}}\Omega \approx 2\pi \times (3\ \text{MHz})$. The intrasite interaction strength $C_6/\ell^6 \approx 2\pi \times (340\ \text{MHz})$. Thus, each of the criteria in equation (2) is satisfied by approximately a factor of ten or more. A realistic cloud geometry, including the relevant length scales for the $n = 33$ state, is shown in figure 2.

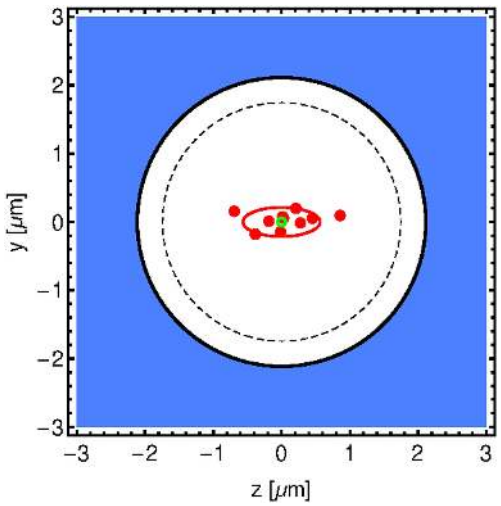

Figure 2. Simulated geometry showing an example atomic distribution for a single lattice site and the relevant length scales for the $33S_{1/2}$ state. The red dots represent $N = 10$ individual atoms while the red ellipse represents the 1σ cloud radii. The outermost contour (solid black line) shows the blockade radius defined as the position where the magnitude of the vdW interactions equals the excitation bandwidth given by the Rabi frequency Ω. The inner dashed contour shows the reduced blockade radius corresponding to the collectively enhanced Rabi frequency $\sqrt{N}\Omega$. The small green circle represents the size of the Rydberg electron wavefunction.

3. Initialisation of collective spin states

To initialise the spin lattice we propose to use collectively enhanced atom–light coupling in each microtrap to drive two-photon Rabi oscillations between the ground state and a state involving a single two-photon Rydberg excitation. Complete population inversion can be realised by interrupting the dynamics after a fixed duration corresponding to a Rabi π-pulse. Recent experiments have demonstrated the preparation of atomic ensemble qubits in this way with an efficiency of

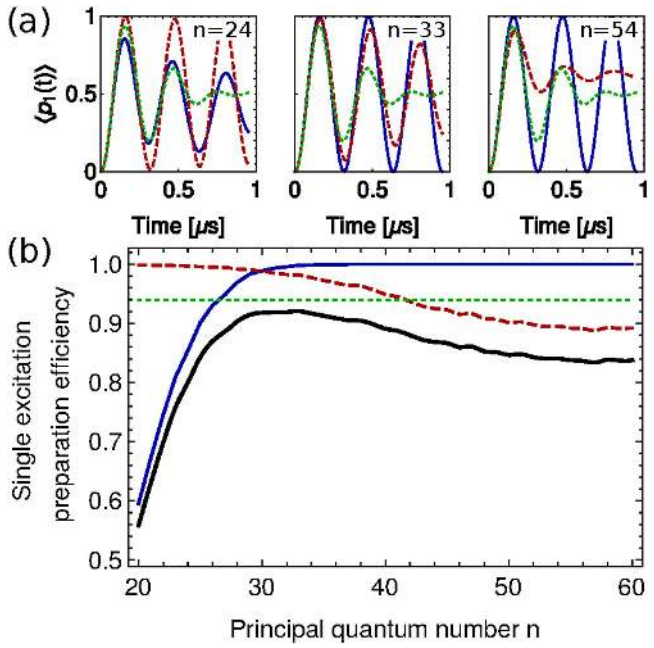

Figure 3. Simulated single-excitation preparation efficiencies for an ensemble of $\bar{N} = 10$ atoms in a microtrap with radii $\sigma_x = \sigma_y = 0.15\ \mu$m, $\sigma_z = 0.4\ \mu$m. The different lines show the effects of Poissonian atom number fluctuations (dotted green), imperfect blockade (solid blue) and short-range physics due to Rydberg electron-atom scattering (dashed red). (a) Calculated Rabi oscillation curves averaged over 1000 random atomic distributions for three different principal quantum numbers: $n = 24$, $n = 33$ and $n = 54$ (from left to right). (b) Single-excitation preparation efficiency as a function of the principal quantum number n. The black line shows the product of the three processes indicating an optimum around $n = 33$ and a combined single-atom preparation efficiency of ≈0.92.

$\langle p_1 \rangle = 0.62$ [29]. However, it is still unclear how much further this can be increased taking into account realistic experimental conditions.

To find conditions which optimise the probability to end the excitation sequence with precisely one Rydberg excitation in each ensemble, we perform numerical simulations of the Rabi dynamics for a small ensemble of atoms resonantly driven to the Rydberg state. Three main mechanisms are assumed which limit the achievable state preparation efficiency: (1) Poissonian atom number fluctuations in each of the magnetic lattice sites due to the stochastic loading process which leads to some disorder in the collective Rabi frequency. (2) Imperfect blockade due to the finite size of the ensemble and the finite range of the nS state van der Waals interactions and (3) short-range physics associated with Rydberg-molecular states. We treat these as independent effects which allows the identification of the dominant limits in an experiment.

Figure 3(b) shows the calculated single excitation preparation efficiency $\langle p_1 \rangle$ in the microtrap containing an average of $\bar{N} = 10$ atoms randomly distributed according to an elongated 3D Gaussian distribution with one-sigma radii $\sigma_z = 0.4\ \mu$m and $\sigma_{x,y} = 0.15\ \mu$m (as shown in figure 2) and averaged over 1000 runs. We assume a resonant single-atom laser coupling with Rabi frequency $\Omega/2\pi = 1$ MHz. The magnetic field is taken to be oriented along z (trap long axis) and for the initial Rydberg state we use $|nS_{1/2}, m_j = 1/2\rangle$, where n is varied in order to obtain the best single excitation preparation efficiency.

The first set of simulations quantifies the role of Poissonian atom number fluctuations assuming perfect Rydberg blockade (horizontal dotted line in figure 3(b)). In this case the dynamics can be reduced to an effective two-level problem with $\sqrt{N}$ enhanced atom–light coupling. The probability to end the sequence with a single excitation oscillates according to $p_1(t) = 1 - \cos^2(\sqrt{N}\Omega t/2)$, see figure 3(a). Assuming N is sampled from a Poisson distribution with mean $\bar{N}$, we calculate the excited-state probability after a time $\tau = \pi/(\sqrt{\bar{N}}\Omega)$ (corresponding to a π-pulse for the collective Rabi oscillations) and average over N. For $\bar{N} = 10$ this gives $\langle p_1(\tau) \rangle = 0.94$ independent of the principal quantum number n (assuming perfect blockade). A simple approximation for the average single-excitation preparation efficiency in the limit $\bar{N} \gg 1$ can be obtained by expanding $p_1(\tau)$ to second order in $N - \bar{N}$ yielding $\langle p_1(\tau) \rangle \approx 1 - \pi^2/(16\bar{N})$.

The second set of simulations concerns the role of the finite size of the ensemble and the imperfect blockade on the efficiency for preparing a single Rydberg excitation (blue solid line in figure 3(b)). Here, we assume each ensemble contains a precise number of atoms randomly distributed within the Gaussian shaped cloud. Interactions between different Rydberg pair states are well approximated by nearly isotropic vdW interactions (figure 2) with coefficients calculated for the $nS_{1/2}$ states of ^{87}Rb for each value of n (see appendix A). The state of the system, including the atom–light coupling, is evolved according to the N-atom Schrödinger equation as a function of time using a reduced Hilbert space truncated at a maximum of three Rydberg excitations in the ensemble. For principal quantum numbers $n \lesssim 30$ the vdW interactions are not sufficient to completely prevent double excitations in the ensemble. This leads to more complicated multilevel Rabi dynamics which after ensemble averaging leads to a damping of the single excitation preparation efficiency.

The third set of simulations takes into account the level shifts induced by the interaction between a Rydberg electron and the surrounding ensemble atoms acting as perturbers in the $nS_{1/2} + 5S_{1/2}$ potential (red dashed line in figure 3(b)). We are not concerned with Rydberg-atom-pair-states (macrodimers) since for the small pair distances within the microtraps there are relatively few pair-states with significant nS character which can be coupled from the ground state and these molecular potential curves are extremely steep leading to a small Frank-Condon factor (see appendix B). Following [30], we calculate the energy shift for a given configuration using the Fermi pseudopotential approach and the measured value of the electron-rubidium s-wave triplet scattering length $a_s = -15.7a_0$ [31]. Higher partial wave scattering is not expected to have a dramatic effect on the short-time Rabi dynamics for the considered densities. The energy shift of the

ensemble for a given configuration of atoms is given by

$$\Delta_R = \frac{2\pi\hbar a_s}{m_e}\sum_i \rho_e(\vec{r}_i - \vec{r}_R), \tag{3}$$

where $\vec{r}_i$ and $\vec{r}_R$ denote the positions of the ground-state atoms and the Rydberg atom, respectively, and m_e is the electron mass. The Rydberg electron probability density $\rho_e(\vec{r}_i - \vec{r}_R)$ at the position of atom i is determined using an analytical approximation to the radial wavefunctions of Rydberg states from quantum defect theory [32] and the spherical harmonic functions for $J = 1/2$, $m_j = 1/2$ states. The Rabi dynamics are then simulated assuming perfect blockade, but where the $(N-1)$-fold excited-state degeneracy is broken by Δ_R. The single-excitation efficiency $p_1(\tau)$ is then simulated numerically and averaged over 1000 random configurations for each value of the principal quantum number n. For $n \lesssim 30$ the probability for two atoms to overlap within the Rydberg orbital radius is vanishingly small, while for $n \gtrsim 38$ electron-atom scattering can significantly reduce the contrast of the collective Rabi oscillations.

Overall these simulations indicate that for the parameters of the magnetic lattice microtraps, the optimal n for maximising the efficiency of initial state preparation for N between 5 and 15 atoms is around $n \approx 33$ with an estimated overall efficiency around $\langle p_1\rangle = 0.92$. This clearly exceeds the classical percolation threshold (indicating the transition to long-range connectivity) for a 2D triangular lattice expected for an occupation probability of 0.5. It is comparable to the state-of-the-art in single-atom preparation in optical microtraps using light-assisted collisions, where efficiencies up to 90% have recently been achieved [33]. Furthermore, the fall-off of the efficiency with n for high n is slow, e.g., the efficiency at $n = 60$ is still 84%. It is likely that the collective state preparation efficiency can be increased to even higher values using, e.g., adiabatic state preparation or composite pulse sequences [34].

4. Long-range spin–spin interactions

Given that the array sites can be initialised with high occupation probability, we now turn to the realisation of lattice spin models where the spin-1/2 degree of freedom is encoded in the collective spin states of equation (1). By using two Rydberg S-states with different principal quantum numbers, i.e., $|R^{\uparrow}\rangle = |n_{\uparrow}S_{1/2}, m_j = 1/2\rangle$ and $|R^{\downarrow}\rangle = |n_{\downarrow}S_{1/2}, m_j = 1/2\rangle$ with $n_{\uparrow} \neq n_{\downarrow}$, one is able to realise a spin-1/2 exchange Hamiltonian [35], with spin–spin couplings of the form

$$H = \sum_{i,j<i}\left[J_z(r_{ij})\mathrm{S}_i^z\mathrm{S}_j^z + \tfrac{1}{2}J_{\perp}(r_{ij})(\mathrm{S}_i^+\mathrm{S}_j^- + \mathrm{S}_i^-\mathrm{S}_j^+)\right] + \sum_i [z_i\tilde{h}_{||}\mathrm{S}_i^z + h_{\perp}\mathrm{S}_i^x - h_{||}\mathrm{S}_i^z]. \tag{4}$$

Here, S_i^z denotes the z-component of the spin-1/2 operator and $\mathrm{S}_i^{\pm}$ is the spin raising/lowering operator at lattice site i. Note that in writing equation (4) we have neglected mixing of Zeeman sublevels which for S-states are two or more orders of magnitude smaller than the coefficients J_z and $J_{\perp}$ (see supplemental material in [11]). Thus, the spin-coupling coefficients are isotropic and only depend on the radial distance between two spins i and j, i.e., $J_z(r_{ij}) = J_z/|r_i - r_j|^6$ and $J_{\perp}(r_{ij}) = J_{\perp}/|r_i - r_j|^6$. The negligible mixing between Zeeman sublevels also allows both Rydberg states to remain magnetically confined in the same potential which will allow for long coherence times.

The coupling constants of equation (4) originate from vdW interactions between the chosen spin states derived in appendix A. For the Ising interaction coefficient we obtain $J_z = C_6(n_{\uparrow}, n_{\uparrow}) + C_6(n_{\downarrow}, n_{\downarrow}) - 2C_6(n_{\downarrow}, n_{\uparrow})$. Here, the $C_6(n_1, n_2)$ coefficients denote the diagonal vdW interaction between the Rydberg states $|n_1S_{1/2}, 1/2\rangle \otimes |n_2S_{1/2}, 1/2\rangle$. The $J_{\perp} = 2\tilde{C}_6(n_{\uparrow}, n_{\downarrow})$ term arises as an exchange process between the degenerate states $|n_{\downarrow}S_{1/2}, 1/2\rangle \otimes |n_{\uparrow}S_{1/2}, 1/2\rangle$ and $|n_{\uparrow}S_{1/2}, 1/2\rangle \otimes |n_{\downarrow}S_{1/2}, 1/2\rangle$ via vdW interactions and strongly depends on $\delta n = n_{\uparrow} - n_{\downarrow}$. The longitudinal field $\tilde{h}_{||} = [C_6(n_{\uparrow}, n_{\uparrow}) - C_6(n_{\downarrow}, n_{\downarrow})]/2$ originates from the small difference between intraspin interactions where z_i is a factor depending on the lattice geometry $z_i = \sum_j r_{ij}^{-6}$. In addition, a tunable microwave field can be applied to couple the $n_{\downarrow}S_{1/2} \leftrightarrow n_{\uparrow}S_{1/2}$ states via a two-photon microwave transition (at a frequency of $1/2 \times 235$ GHz for $n = 33$) giving rise to tunable longitudinal and transverse field terms $h_{\perp}$ and $h_{||}$.

The Hamiltonian of equation (4) allows to study anisotropic XXZ spin-1/2 models in various geometries with additional longitudinal and transverse fields. This has applications in understanding the magnetic properties of materials like Cs_2CoCl_4 [36, 37] and allows to study exotic quantum phases of matter [38]. In the absence of the transverse field, i.e., $h_{\perp} = 0$, the Hamiltonian has $U(1)$ symmetry and conserves the total magnetisation $M_z = \sum_i \mathrm{S}_i^z$. This limit has been studied extensively in *one-dimensional* spin chains with next-neighbour interactions and it can be solved exactly using the Bethe ansatz [39]. It supports three quantum phases depending on the anisotropy ratio $\Delta = J_z/J_{\perp}$: (i) A ferromagnetic phase for $\Delta < -1$ with a classical ferromagnetic ground state gapped from other states, (ii) a gapless Luttinger-liquid for $-1 < \Delta < 1$ with a spin-liquid ground state and a power-law decay of correlations, and (iii) an Ising-like region for $\Delta > 1$ with an antiferromagnetic phase along the z-direction and a gap in the excitation spectrum. In the special case $\Delta = 1$ the system realises a Heisenberg model with $SU(2)$ symmetry.

For the anisotropic XXZ spin-1/2 model in *two dimensions*, there exists no exact solution, but it is expected that it supports non-trivial quantum phases which depend on the lattice geometry. For example, on a triangular lattice it gives rise to a stable supersolid phase [40, 41] while on a kagome lattice a spin-singlet valence-bond solid phase emerges [42–44]. In addition, due to the $1/r^6$ character of the spin–spin interactions one can realise frustrated $J - J'$ models on a square (or rhombus) lattice which are expected to yield stable stripe-like supersolid phases [38, 45]. In general, integrability is lost when a transverse magnetic field is added $h_{\perp} \neq 0$ which breaks the $U(1)$ symmetry and the conservation of the total magnetisation. It is expected that both in the ferromagnetic and antiferromagnetic phase a quantum phase transition

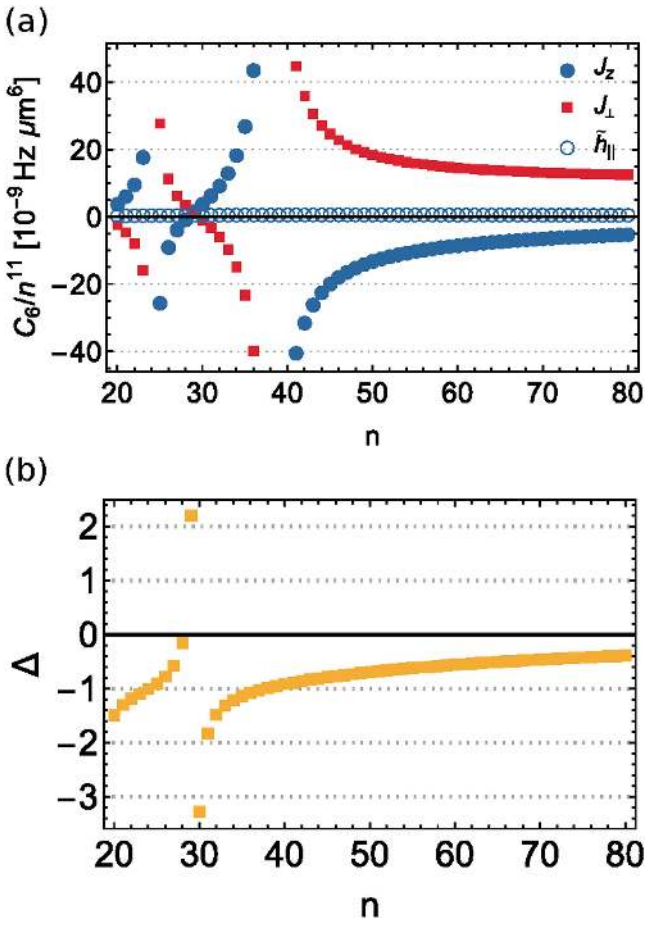

Figure 4. (a) Spin–spin interaction coefficients of equation (4) as a function of principal quantum number n for the $nS_{1/2}$ and $(n+1)S_{1/2}$ states, and (b) anisotropy ratio $\Delta = J_z/J_\perp$.

to a paramagnetic phase in the x-direction appears at a critical value $h_\perp^c$ and that in the Luttinger-liquid region a gap opens [46, 47].

As a particular example to demonstrate the tunability of the resulting spin interactions we discuss the case $n_\uparrow = n_\downarrow + 1$ (i.e., $\delta n = 1$) for which the exchange process $J_\perp$ is maximised. (See appendix A, figure 7 for $\delta n = 2$ and 3.) Figure 4 shows the numerically calculated coupling strengths for $nS_{1/2}$ and $(n+1)S_{1/2}$ states (upper panel) and the resulting anisotropy parameter $\Delta = J_z/J_\perp$ (lower panel) as a function of the principal quantum number n. Both J_z and $J_\perp$ show two definite Förster resonances around $n \approx 24$ and $n \approx 38$ where the channels to $\{nP_{3/2}, nP_{1/2}\}$ and $\{nP_{3/2}, nP_{3/2}\}$ states become close in energy, respectively. Apart from $n \sim 28$ the longitudinal field $\tilde{h}_{||}$ is negligible compared to J_z and $J_\perp$. Due to these two resonances it is possible to realise ferromagnetic J_z interactions for $n \in \{25, 28\}$ and $n > 38$ or antiferromagnetic spin interactions for $n < 25$ and $n \in \{29, 38\}$. The anisotropy parameter Δ exhibits a resonance around $n = 30$ and crosses the transition from ferromagnetic to spin-liquid phases at $n = 40$ ($\Delta = -1$).

The inclusion of a tunable microwave field allows for further control, including time-dependent control of transverse and longitudinal fields. In a typical experiment one will start with all spins initialised in the $n_\downarrow S_{1/2}$ state. This is the ground state of the system for $h_{||} \to -\infty$. Suddenly switching on the microwave field at resonance will realise a quantum quench in which the competition between the transverse field and the interstate spin–spin interactions leads to complex dynamical behaviour [48]. Alternatively, the microwave field could be ramped slowly (starting far below resonance $h_\perp = 0$, $h_{||} \ll 0$) to different points of the phase diagram to prepare exotic ground states in an adiabatic fashion. This would be particularly interesting for 1D and 2D spin-1/2 XXZ models in frustrated geometries in coexisting longitudinal and transverse magnetic fields.

Even more diverse spin models are possible if the spin degrees of freedom are encoded in two Rydberg P-states giving rise to anisotropic spin models including generalised compass type models [49]. In this case the spins can be encoded in the Rydberg nP, $m_j = +1/2$ and $m_j = -1/2$ states (see appendix C), which can be reached by single-step excitation from the ground state. However, while the $m_j = +1/2$ state can be trapped in a magnetic lattice, the $m_j = -1/2$ state is a high field-seeking state ($m_j g_j = -1/3$). We estimate that the time scale associated with the atomic motion in the steep anti-trapping potential for the nP, $m_j = -1/2$ state is around 5–10 μs, which is significantly shorter than the lifetime of the Rydberg states ($\sim$50 μs for $n = 40$). Such models could instead be implemented in large period optical lattices.

For the proposed experiments it is likely that spatial disorder will be a significant factor. For the parameters considered in our magnetic lattice the ensembles have a mean radius of 0.21 μm. For a 2.5 μm period magnetic lattice this will lead to a variation in nearest neighbour distances of about 8%. Due to the strong r^{-6} scaling of the vdW interactions this leads to a variation in nearest-neighbour coupling strength of about 50%. While some features of the quantum phase structure may be insensitive to this disorder, it is an open question to what extent this disorder may influence spin dynamics [50].

5. Readout of spin–spin correlations

To read out the spin state in each microtrap with high fidelity we propose a triggered ionisation avalanche detection scheme which exploits each atomic ensemble as a highly sensitive amplifier. It is similar in spirit to readout schemes based on interaction enhanced imaging [51, 52] or conditional Raman transfer of the ensemble of atoms between ground states proposed in [19]. Although the ionisation approach is inherently destructive, it may be more robust than other schemes that rely on coherent control of Rydberg states and it does not require that the participating states remain magnetically trapped. Similar ionisation avalanche processes have already been observed in experiments, and appear to be a very rapid way to empty a trap of atoms [26]. We propose the following experimental procedure (graphically depicted in figure 5):

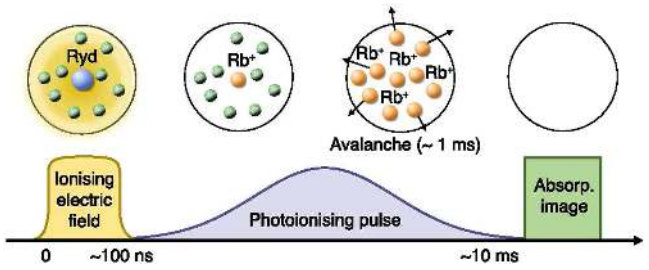

Figure 5. Schematic of the single Rydberg-atom triggered ionisation avalanche scheme in which the presence of a single Rydberg atom in a given spin state conditionally transfers a large number of ground-state atoms in the trap to an untrapped state via a seeded photoionisation avalanche. Site-resolved spin–spin correlations can then be directly measured via absorption imaging of the remaining filled (or empty) sites.

5.1. Spin-selective optical pumping

First, a single spin state must be selected for detection. This is possible by coupling the $n_{\downarrow}S_{1/2}$, $m_j = +1/2$ spin-down state to a lower short-lived state, such as the $5P_{3/2}$ state (which spontaneously decays with a lifetime 26 ns) via a resonant laser field at 480 nm (depicted in figure 1, inset). In this way the $n_{\downarrow}S_{1/2}$, $m_j = +1/2$ population can be optically pumped with a fidelity >95% within 100 ns, leaving only the spin-up state in the trap.

5.2. Pulsed field ionisation

Next an electric field pulse with a short duration ~100 ns is applied with a field strength of approximately $F = 400$ V cm^{-1}. This is sufficient to suddenly field-ionise the remaining Rydberg atoms (figure 6). This pulse is long enough to eject the electron but short enough that the force on the produced Rydberg ions does not displace them far from the vicinity of their original microtraps. We estimate the escape time for an ion as several microseconds. These 'seed' ions produce a spatially inhomogeneous electric field which decays with distance r according to $q/(4\pi\epsilon_0 r^2)$, with q the elementary charge and ϵ_0 the vacuum permittivity.

5.3. Seeded photoionisation avalanche

The 780 + 480 nm laser pulses are then immediately applied to the whole lattice for several milliseconds. The spatially inhomogeneous field originating from the seed ions shifts the ionisation thresholds for the remaining ground-state atoms such that they can be photoionised (figure 5). This rapidly produces more ions which escape the magnetic trap until it is emptied. The classical field-ionisation limit, given by $E_c = -2\sqrt{F}$ (atomic units), for an energy corresponding to the $33S_{1/2}$ state corresponds to a field strength of $F = 400$ V cm^{-1}. At or above this field strength it should be very efficient to excite the remaining ground state atoms to unbound continuum states by turning the Rydberg excitation lasers back on. This is a convenient value which falls between the field strength for atom-ion separations given by the Wigner-Seitz radius and the trap length $l = 0.8$ μm (640 V cm^{-1} or 25 V cm^{-1}, respectively). Early studies of strong field photoionisation of rubidium atoms using pulsed laser fields found rates exceeding 5×10^4 s^{-1} [53], indicating that the entire trap could be photoionised in this way within a few milliseconds. To ensure there is no crosstalk between the traps we require that the electric field originating from one trap is sufficiently small at neighbouring traps to suppress photoionisation. This is satisfied for a $a = 2.5$ μm period lattice, for which the ion-produced field of 2.3 V cm^{-1} is more than 100 times smaller than the classical field ionisation limit for the $33S_{1/2}$ state (assuming a single charged particle).

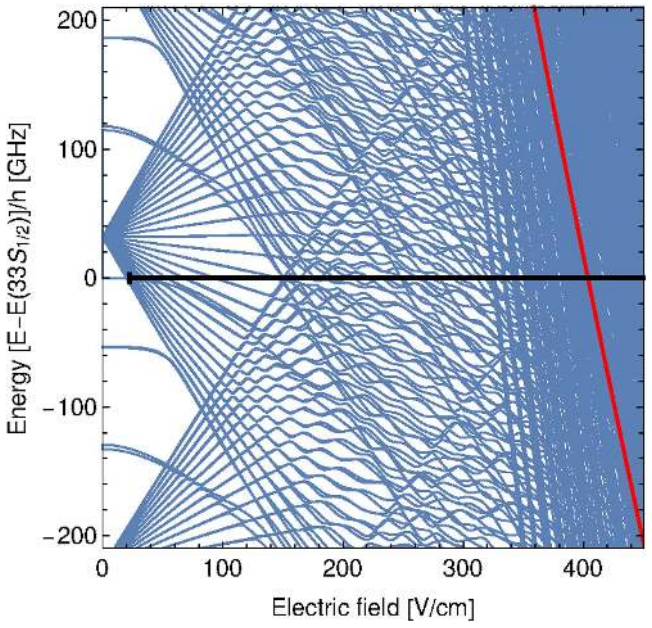

Figure 6. Energy as a function of electric field (Stark map) around the $33S_{1/2}$ state of rubidium. The red diagonal line shows the classical field-ionisation threshold. A single ion in the microtrap produces a spatially inhomogeneous electric field which decays as $1/r^2$ and ranges from 22.5 V cm^{-1} (corresponding to $r = l = 0.8$ μm) to above the classical field-ionisation threshold, to 640 V cm^{-1} for distances corresponding to the Wigner-Seitz radius $r = 0.15$ μm as shown by the black horizontal bar. The electric field strength at neighbouring traps $F = 2.3$ V cm^{-1} is well below the classical field-ionisation threshold.

5.4. Absorption imaging of the remaining atoms

To measure the magnetisation and spin–spin correlations across the magnetic lattice, standard *in situ* reflection absorption imaging used for atom chips can be employed [14, 16, 17], in which a strongly absorbing or a non-absorbing site signifies $|\downarrow\rangle$ or $|\uparrow\rangle$, respectively. Sensitive absorption imaging down to fewer than 10 atoms in each site of a magnetic lattice has already been demonstrated [14].

In this way it will be possible to read out the S^z projection of the spin state in each site of the whole lattice. By repeating such experiments it will then be straightforward to calculate spin–spin correlations, such as the pairwise correlation function $\langle S_i^z S_j^z \rangle$ or even higher order correlation functions, which is sufficient to identify spin-liquid behaviour [54]. The time resolution, which is determined by the time required to optically pump and field-ionise the remaining

Rydberg state (thereby freezing the spin dynamics), is almost an order of magnitude shorter than the expected time scale for nearest-neighbour spin exchange ($\sim$1 μs). To control errors due to imperfect initialisation or loss from the Rydberg state during evolution it could be advantageous to repeat the whole detection process by optical pumping the other spin state.

6. Additional experimental considerations

6.1. Magnetic lattices

In a magnetic lattice, atoms oriented in low magnetic field-seeking states ($m_F g_F > 0$) are repelled by the increasing magnetic field in the traps allowing these atoms to be trapped in the magnetic field minima. For the Rydberg states, we choose $nS_{1/2}$, $m_j = +1/2$ and $(n+1)S_{1/2}$, $m_j = +1/2$, such that they experience similar magnetic trapping potentials. The algorithm of Schmied *et al* [15] can be used to design optimised magnetic microstructures to create 2D magnetic lattices of various geometries, including those proposed in section 4. Magnetic lattices can be readily constructed with a large lattice spacing which allows atomic ensembles in individual sites to be easily resolved *in situ* using standard optical imaging.

For the quantum simulation of lattice spin models we envisage initially creating a 5×5 mm^2, 2.5 μm period triangular magnetic lattice using magnetic microstructures fabricated by electron beam lithography and reactive ion etching of a 100 nm thick multi-atomic-layer Co/Pd film [18]. These films have a large perpendicular magnetic anisotropy, high saturation magnetisation ($\sim$5.9 kG) and coercivity ($\sim$1 kOe), a very small grain size ($\sim$7 nm), and are capable of producing magnetic microstructures with very homogeneous magnetic potentials [18]. We have simulated a triangular lattice based on the code of Schmied *et al* [15]. The trap symmetry and depth is optimal for a trap height $a/2$ above the magnetic microstructure. For in-plane and perpendicular bias fields of $B_\perp = 12$ G and $B_\parallel = 1.4$ G the corresponding magnetic traps are cigar-shaped with radial and axial trap frequencies $\omega_{\rm rad}/2\pi = 114$ kHz and $\omega_{\rm ax}/2\pi = 36$ kHz and a trap depth of 7.7 G (260 μK for $F = 1$, $m_F = -1$). The Ioffe field $B_{\rm Ioffe} = 4.6$ G is oriented along the trap long axis which is tilted at an angle of $\psi = 5\pi/12$. Based on our recent experience with one-dimensional magnetic lattices [17], we expect about 10^6 ^{87}Rb atoms in the $|F = 1, m_F = -1\rangle$ low field-seeking state can be loaded to the central 200×200 sites of the triangular magnetic lattice using a Z-wire microtrap. With a subsequent radio-frequency evaporative cooling phase we anticipate that each lattice site may be populated by approximately 10 atoms at a temperature of $\sim$1 μK.

6.2. Surface effects

A potential issue when using long-range interacting Rydberg atoms stored in a magnetic lattice is the effect of the atom chip surface on the Rydberg atoms, which are trapped at a height of typically one-half of a lattice spacing from the magnetic surface [25]. A main concern is that following each cooling and trapping sequence alkali atoms can stick to the surface of the atom chip to create inhomogeneous electric fields. The valence electron of each adsorbed atom can reside partially inside the metal surface and the charge separation creates a dipole whose strength is related to the difference between the work function of the metal (5.1 eV for gold) and the ionisation potential of the atoms (4.2 eV for Rb) [55]. The dipoles produce inhomogeneous electric fields that can perturb the nearby Rydberg atoms [15]. Studies of Rb Rydberg atoms trapped at distances down to 20 μm from a gold-coated atom chip surface have revealed small distance-dependent energy shifts of $\sim\pm$10 MHz for $n \approx 30$ [56]. While this could influence the fidelity of initial state preparation, we do not expect it to have a dramatic effect on the subsequent spin models since the nS and $(n+1)S$ Rydberg states are almost insensitive to electric fields due to their small differential electric polarizability. Recent studies have demonstrated that the stray electric fields can be effectively screened out by depositing a thin ($\sim$90 nm) uniform film of Rb ($\varphi = 2.3$ eV) over the entire gold surface of a cryogenic atom chip [57] or by using a smooth monocrystalline quartz surface film coated with a monolayer of Rb adsorbates [58]. Another potential issue is the effect of the 480 nm beam when the beam is parallel to the chip surface at a height of about one-half of a lattice spacing. Further work will be required to fully understand and control these surface effects.

7. Summary and outlook

We have proposed a scheme to simulate lattice spin models based on the use of strong, long-range interacting Rydberg atoms stored in a large-spacing magnetic lattice. We point out, however, that these ideas could equally well be implemented in large-period optical lattices. Each spin is encoded directly in a collective spin state involving a single nS or $n'S$ Rydberg atom in an ensemble of ground-state rubidium atoms prepared via Rydberg blockade. The Rydberg spin states on neighbouring lattice sites are allowed to interact with the driving fields turned off. Afterwards they are read out using a single-Rydberg atom triggered photoionisation avalanche scheme in which the presence of a single Rydberg atom conditionally transfers a large number of ground-state atoms in the trap to untrapped states which can be readily detected by standard site-resolved absorption imaging.

The use of Rydberg states leads to spin–spin coupling strengths which are much larger than the relevant decoherence rates and provides a way to design and realise complex spin models including XXZ-type spin models. This paves the way towards engineering exotic spin models, such as spin models based on triangular-based lattices which can give rise to a rich quantum phase structure including frustrated-spin states. Experiments could probe spin–spin correlations on different spatial scales which can be compared with theoretical descriptions to reveal the universal characteristics of these systems including ground-state properties, critical exponents and relaxation dynamics.

In addition to the ground-state phase diagram, this quantum simulator is suited to study transient many-body phenomena. Given that the lifetimes of the high Rydberg states are typically >100 μs and the characteristic time-scale associated with spin–spin interactions is ~ 1 μs it should be possible to investigate dynamics on both short and long time scales. In particular, it should be possible to investigate the build-up of spin–spin correlations on different length and time scales following a dynamical change in the system parameters, including their dependence on the transition rate which can be compared with, for example, the Kibble-Zurek scaling law for a system driven through a continuous phase transition at finite rate [48]. Other interesting questions that could be addressed are how long and by what path does a far-from-equilibrium isolated quantum system take to reach an equilibrium state? and is it possible to connect certain non-equilibrium properties to the properties of the ground state?

Acknowledgments

We are indebted to Peter Zoller for helping initiate this project. We also thank Rick van Bijnen for use of his code for calculating Rydberg–Rydberg interaction potentials shown in figure 8, Tien Tran for calculating the magnetic lattice parameters and Adrien Signoles and Yun Li for stimulating discussions. This work is supported by an Australian Research Council Discovery Project grant (DP130101160). SW acknowledges support by the Heidelberg Center for Quantum Dynamics, the European Union H2020 FET Proactive project RySQ (grant No. 640378), the Deutsche Forschungsgemeinschaft under WH141/1-1 and the DFG Collaborative Research Centre 'SFB 1225 (ISOQUANT)'. AWG acknowledges support from the SFB FoQuS (Austrian Science Fund FWF Project No. F4016- N23), the European Research Council Synergy Grant UQUAM and a Swinburne University Visiting Researcher grant.

Appendix A. Rydberg interaction between ^{87}Rb atoms in $n_1S_{1/2}$ and $n_2S_{1/2}$ Rydberg states

In assessing the relevant interactions between Rydberg states we distinguish between two main regimes: (i) long-range van der Waals interactions, (ii) cross over to dipole–dipole interactions and avoided crossings.

For distances large enough, such that the dipole interaction matrix element between two S-states and two P-states is larger than the energy difference Δ_F between these pair states, i.e., $V_{\rm dip} > \Delta_F$, we can treat vdW interactions perturbatively. The vdW interaction Hamiltonian between $n_1S_{1/2}$ and $n_2S_{1/2}$ Rydberg states both in the Zeeman sublevel $m_j = +1/2$ can be described by a 4×4 matrix of the form

$$H_{\rm int} = \begin{pmatrix} C_6(n_1, n_1) & 0 & 0 & 0 \\ 0 & C_6(n_1, n_2) & \tilde{C}_6(n_1, n_2) & 0 \\ 0 & \tilde{C}_6(n_2, n_1) & C_6(n_2, n_1) & 0 \\ 0 & 0 & 0 & C_6(n_2, n_2) \end{pmatrix}. \tag{A1}$$

The vdW coefficients are given by

$$\begin{aligned} C_6(n_1, n_2) &= \langle n_1S_{1/2}1/2,\, n_2S_{1/2}1/2|H_{\rm vdW}|n_1S_{1/2}1/2,\\ &\quad n_2S_{1/2}1/2\rangle \\ \tilde{C}_6(n_1, n_2) &= \langle n_1S_{1/2}1/2,\, n_2S_{1/2}1/2|H_{\rm vdW}|n_2S_{1/2}1/2,\\ &\quad n_1S_{1/2}1/2\rangle. \end{aligned} \tag{A2}$$

with the vdW interaction operator

$$H_{\rm vdW} = \sum_{n,j,m_j n',j',m'_j} \frac{V_{\rm dd}|nP_jm_j,\, n'P_{j'}m'_j\rangle \langle nP_jm_j,\, n'P_{j'}m'_j|V_{\rm dd}}{E_{n_1} + E_{n_2} - E_n - E_{n'}}, \tag{A3}$$

coupling S-states with energies E_{n_1} and E_{n_2} to intermediate P-states with energies E_n and $E_{n'}$ via dipole–dipole interactions

$$V_{\rm dd}(\mathbf{r}) = -\sqrt{\frac{24\pi}{5}} \frac{1}{r^3} \sum_{\mu,\nu} C^{1,1;2}_{\mu,\nu;\mu+\nu} Y_2^{\mu+\nu}(\vartheta,\, \varphi)^* d_\mu d_\nu.$$

Here, $\mathbf{d}$ is the atomic dipole operator and $\mathbf{r} = (r,\, \vartheta,\, \varphi)$ is the vector between the two atoms in spherical coordinates. With d_μ we denote the μth spherical components ($\mu,\, \nu \in \{-1,\, 0,\, 1\}$) of the atomic dipole operator, $C^{j_1,j_2;J}_{m_1,m_2;M}$ are Clebsch–Gordan coefficients and Y_l^m are spherical harmonics.

The resulting spin–spin interactions from equation (A1) between two atoms separated by a distance a are

$$\begin{aligned} J_z &= [C_6(n_1, n_1) + C_6(n_2, n_2) - 2C_6(n_1, n_2)]/a^6, \\ J_\perp &= 2\tilde{C}_6(n_1, n_2)/a^6, \\ h_{||} &= [C_6(n_1, n_1) - C_6(n_2, n_2)]/(2a^6). \end{aligned} \tag{A4}$$

Figures 4 and 7 show the resulting spin-coefficients for $n_2 - n_1 = 1$ and $n_2 - n_1 = 2$ or 3, respectively, which agree well with [35].

Appendix B. Short-range physics

The perturbative treatment giving rise to vdW interactions becomes increasingly inaccurate for small interatomic distances, e.g., for $d < 1$ μm and $n \approx 30$. In order to obtain the interaction potentials in the regime of small interatomic distances, $d < 1$ μm, but still large enough such that the Rydberg orbits of size $R_{\rm ryd} \sim a_0 n^2$ do not overlap, $R_{\rm ryd} \ll d$, we diagonalise the dipole–dipole interaction Hamiltonian using 10^4 basis states. Figure 8(a) shows a typical example of interaction potentials around the $2 \times 36P$ Rydberg states of ^{87}Rb for $\vartheta = \pi/2$ and a magnetic field splitting of 20 MHz (14.3 G). Panels (b), (d) show a magnification of the interaction potentials around the $2 \times 36P_{1/2}$ Rydberg state. The colour code indicates the overlap

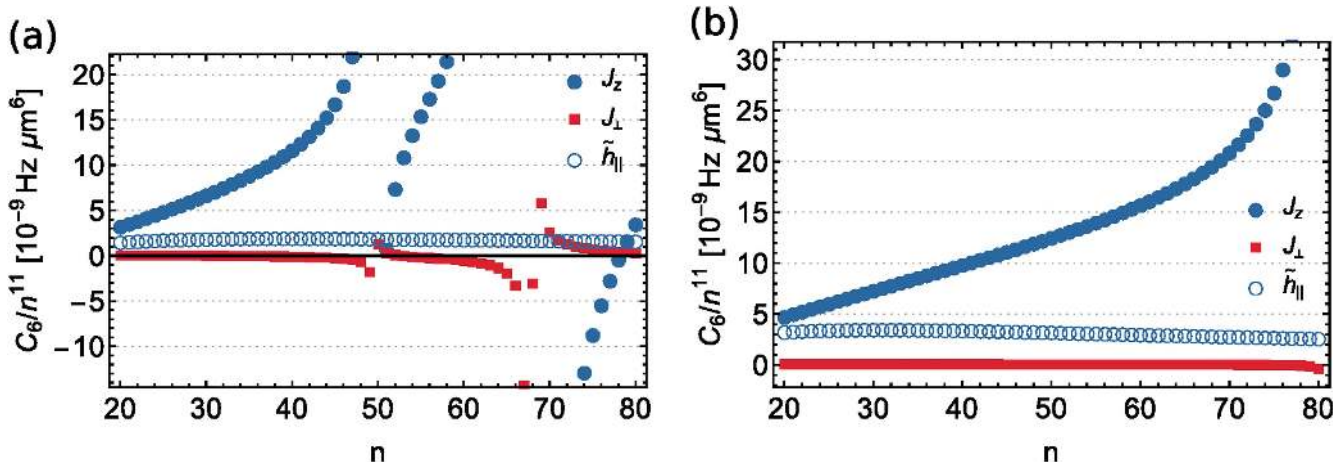

Figure 7. Spin–spin interaction coefficients of equation (4) as a function of principal quantum number n for the (a) $nS_{1/2}$ and $(n+2)S_{1/2}$ and (b) $nS_{1/2}$ and $(n+3)S_{1/2}$ Rydberg states.

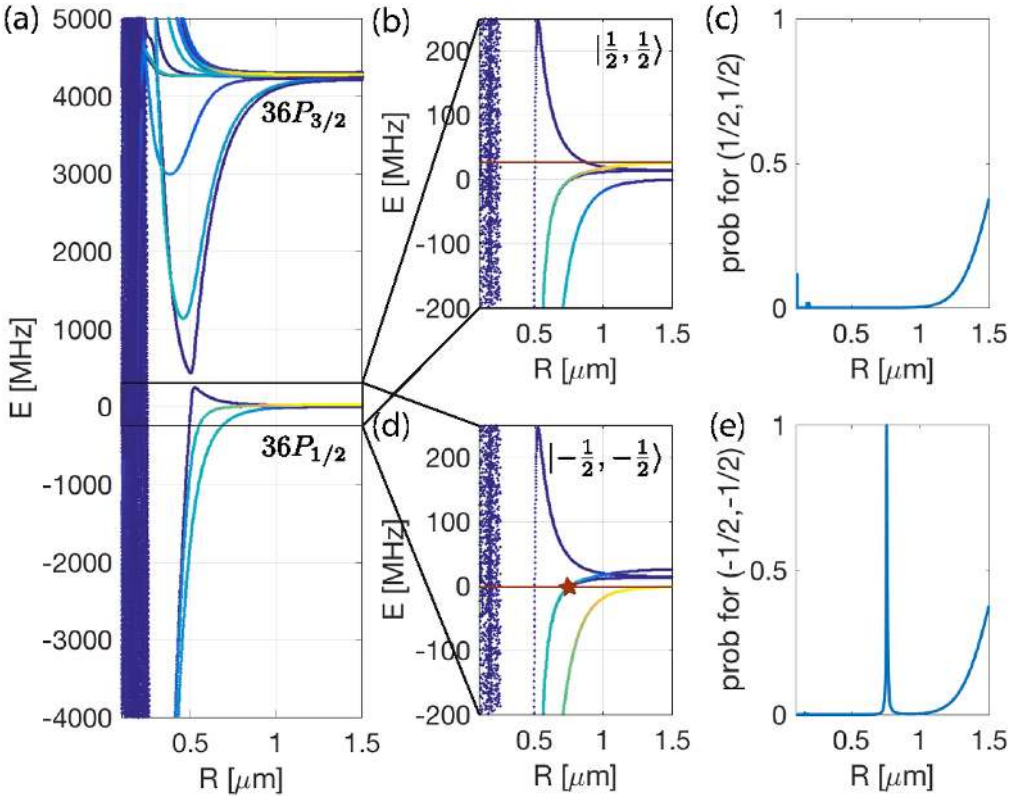

Figure 8. (a) Born–Oppenheimer interaction potentials around the $2 \times 36P_{1/2}$ Rydberg states for a magnetic field splitting of 20 MHz as a function of distance. (b), (d) Magnification of the interaction potentials. The red line corresponds to the laser excitation energy. The colour quantifies the contribution of the $\left|\frac{1}{2}\frac{1}{2}\right\rangle$ (panel (b)) and $\left|-\frac{1}{2}-\frac{1}{2}\right\rangle$ (panel (d)) Zeeman sublevels to the Born–Oppenheimer eigenstates. (c), (e) Excitation probability for double-excited Rydberg states.

of the Born–Oppenheimer eigenstates with the $\left|\frac{1}{2}\frac{1}{2}\right\rangle = |36P_{1/2}, m_j = 1/2, 36P_{1/2}, m_j = 1/2\rangle$ state (panel (b)) or with the $\left|-\frac{1}{2}-\frac{1}{2}\right\rangle = |36P_{1/2}, m_j = -1/2, 36P_{1/2}, m_j = -1/2\rangle$ state (panel (d)). For distances smaller than 1 μm the states $\left|-\frac{1}{2}-\frac{1}{2}\right\rangle$ and $\left|\frac{1}{2}\frac{1}{2}\right\rangle$ start to mix. Panels (c), (e) show the excitation probability of a laser resonant with the $\left|\frac{1}{2}\frac{1}{2}\right\rangle$ (panel (c)) or the $\left|-\frac{1}{2}-\frac{1}{2}\right\rangle$ (panel (e)) states as a function of the interatomic separation. For large separation and vanishing interaction energy both probabilities approach unity, while for small interatomic separations the excitation probability should vanish due to the

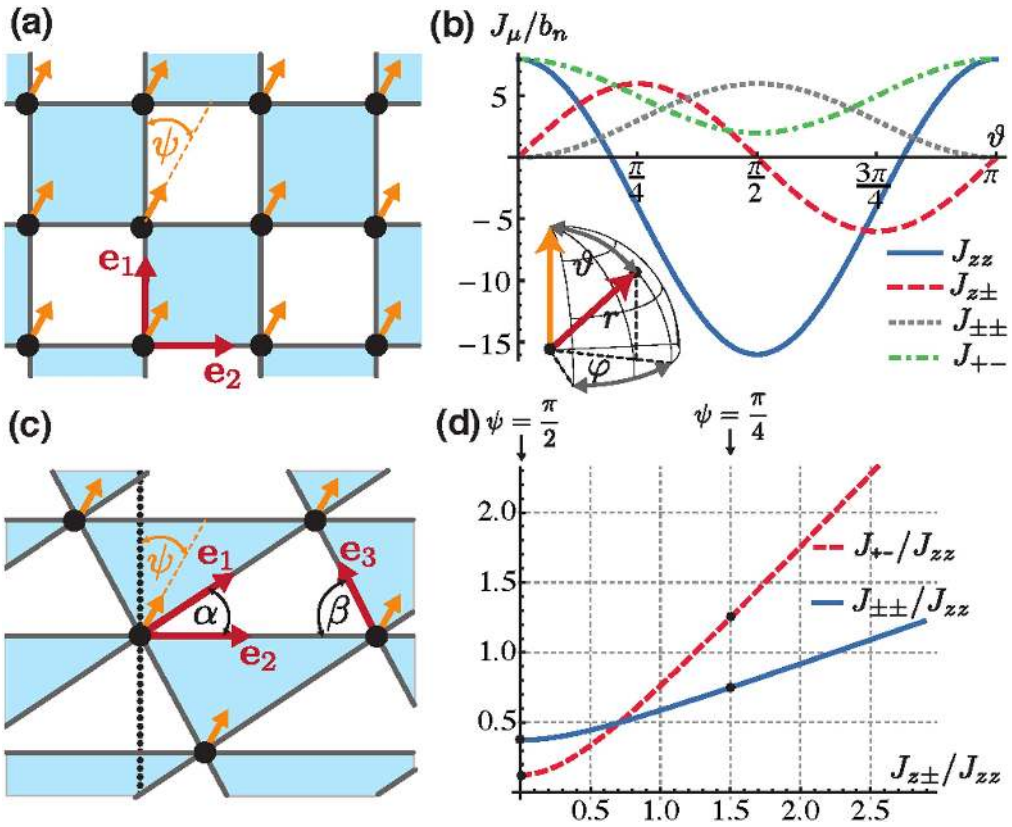

Figure 9. Tuning of anisotropic spin–spin interactions via the lattice symmetry and quantisation axis. (a) Spins (black dots) located on a rectangular lattice with orthogonal bond directions $\mathbf{e}_1$ and $\mathbf{e}_2$ (red arrows) and quantisation axis tilted by an angle ψ (yellow arrow). (b) Interaction coefficients of equation (C2) as a function of ϑ. (c) Spins (black dots) on a non-equilateral triangular lattice with three bond directions $\mathbf{e}_1$, $\mathbf{e}_2$ and $\mathbf{e}_3$ (red arrows) and in-plane quantisation axis tilted by an angle ψ (yellow arrow). (d) Variation of the relative strength of the interaction coefficients of equation (C2) as a function of ψ for bond 1 of the square lattice.

Rydberg blockade effect. However, it could happen that at short distances accidental resonances lead to resonant pair excitations. Taking into account 10^4 Rydberg states, panels (c), (e) show that the excitation probability due to the very small overlap of the wavefunctions is negligible even for distances as large as 1 μm. In panel (e) we observe 'magic distances' [59] at around 0.68 μm (red star in panel (d)). This resonance occurs due to the fact that one couples to Zeeman states with the lowest energy and thus resonantly hits the (attractive) Born–Oppenheimer potential which asymptotically connects to the $\left|\frac{1}{2}\frac{1}{2}\right\rangle$ Rydberg states but at short distances contains a significant contribution of the $\left|-\frac{1}{2}-\frac{1}{2}\right\rangle$ Rydberg state. These resonances can be avoided by using the right combination of laser polarisation and magnetic field direction.

Appendix C. Long-range and anisotropic spin–spin interaction with Rydberg $nP_{1/2}$ states

With Rydberg $nP_{1/2}$ states one is able to realise the most general spin-1/2 exchange Hamiltonian where spin degrees of freedom are encoded in the two Zeeman sublevels and vdW interactions give rise to spin–spin interactions of the form [11, 59]

$$\begin{aligned} H = \frac{1}{2}\sum_{\mu}\sum_{i,j\in\mu}\frac{1}{r_{ij}^6}[&J_{zz}^{(\mu)}(\vartheta_\mu)\mathsf{S}_i^z\mathsf{S}_j^z \\ &- J_{+-}^{(\mu)}(\vartheta_\mu)(\mathsf{S}_i^+\mathsf{S}_j^- + \mathsf{S}_i^-\mathsf{S}_j^+) \\ &+ J_{\pm\pm}^{(\mu)}(\vartheta_\mu)(e^{-2i\varphi}\mathsf{S}_i^+\mathsf{S}_j^+ + e^{2i\varphi}\mathsf{S}_i^-\mathsf{S}_j^-) \\ &+ J_{z\pm}^{(\mu)}(\vartheta_\mu)[\mathsf{S}_i^z(e^{-i\varphi}\mathsf{S}_j^+ + e^{i\varphi}\mathsf{S}_j^-) + \text{h.c.}]]. \end{aligned} \tag{C1}$$

Here, S_i^z denotes the z-component of the spin-1/2 operator and $\mathsf{S}_i^\pm$ denotes the spin raising/lowering operator at lattice site i while (r, ϑ, φ) are the spherical components of the vector connecting spins i and j. With μ we denote the bond of the lattice along the unit vector $\mathbf{e}_\mu$ as illustrated in figure 9. For a square lattice $\mu \in \{1, 2\}$ while for the triangular lattice $\mu \in \{1, 2, 3\}$, see panels (a) and (c) of figure 9, respectively. The coupling constants of equation (C1) are given by

$$\begin{aligned} J_{zz}^{(\mu)}(\vartheta) &= [12\cos(2\vartheta) - 4]\, b_n, \\ J_{+-}^{(\mu)}(\vartheta) &= [3\cos(2\vartheta) + 5]\, b_n, \\ J_{\pm\pm}^{(\mu)}(\vartheta) &= 6\sin^2(\vartheta)\, b_n, \\ J_{z\pm}^{(\mu)}(\vartheta) &= 6\sin(2\vartheta)\, b_n, \end{aligned} \tag{C2}$$

with $b_n > 0$ (for $nP_{1/2}$ states) being generalised vdW coefficients which determine the overall sign and strength of the spin–spin interactions. The angle ϑ is the angle between the quantisation axis (yellow arrow) and the vector connecting the two atoms (red arrow) along the bond μ, see inset in figure 9(b). The model Hamiltonian of equation (C1) can serve as a toolbox for studying general spin–spin models in which the nature of the couplings can be different along different lattice directions.

As a particular example to demonstrate the tunability of the resulting spin interaction toolbox we discuss square and triangular lattices. In the conceptionally simplest case where the quantisation axis defined by the magnetic field direction at the trap bottom is aligned perpendicular to the 2D chip ($\vartheta = \pi/2$), we obtain an XXZ model with $J_{zz} = -16b_n$, $J_{\pm\pm} = 6b_n$, $J_{+-} = 2b_n$ and $J_{z\pm} = 0$ independent of the bond direction and lattice geometry. For $b_n > 0$ it supports a ferromagnetic ground state which competes with the $J_{\pm\pm}$ term which tries to 'melt' the ferromagnet through pair-correlated spin flips. By breaking the lattice symmetry (e.g., moving to rectangular or non-equilateral triangle lattices) one can tune the relative strength of the interaction coefficients along different bond directions due to the strong $1/r^6$ dependency. Additionally, the effects of the $J_{\pm\pm}$ terms can be suppressed by increasing the magnetic field at the trap bottoms which results in an excitation energy gap for non-spin conserving terms.

Even richer spin models can be studied by aligning the quantisation axis in-plane giving rise to anisotropic spin models for various geometries, where the interaction coefficients of equation (C2) vary as a function of the bond directions labelled by $\mathbf{e}_\mu$. We first consider the square lattice of figure 9(a) with orthogonal bond directions $\mathbf{e}_1$ and $\mathbf{e}_2$ and an in-plane quantisation axis tilted by an angle ψ. The relative angles for the two bonds $\mu = 1, 2$ of equation (C1) are $\vartheta_1 = \psi$ and $\vartheta_2 = \pi/2 - \psi$. In the special case of $\psi = 0$ the resulting spin–spin interactions for the first bond (i.e., $\vartheta_1 = 0$) correspond to an XXZ Hamiltonian with $J_{zz} = J_{+-}$ and $J_{\pm\pm} = J_{z\pm} = 0$. However, for the second bond direction $\vartheta_2 = \pi/2$, which gives rise to additional $J_{\pm\pm}$ terms (figure 9(b)). By rotating the quantisation axis such that $\psi > 0$ one can increase the $J_{\pm\pm}$ and $J_{z\pm}$ coefficients at the expense of J_{zz} and J_{+-}, thus offering the possibility to explore the rich phase structure of spin models with anisotropic couplings which are expected to exhibit a variety of non-trivial ground states [60, 61]. This is illustrated for the first bond direction of the square lattice in figure 9(d) where by changing ψ from $\pi/5$ to $\pi/2$ one can change the interaction coefficients according to equation (C2) over a wide range.

For the triangular lattice illustrated in figure 9(c) one can implement spin models where the interaction coefficients of equation (C2) depend on all three bond directions $\mu = 1, 2, 3$ with $\vartheta_1 = \pi/6 - \psi$, $\vartheta_2 = \pi/2 - \psi$ and $\vartheta_3 = \pi/6 + \psi$. Thus, Rydberg spins in microtrap arrays may serve as the first concrete realisation of exotic spin models such as generalised compass type models [49]. This could be of importance for understanding non-trivial phases of frustrated magnetism in which the competition between spin–spin interactions cannot be simultaneously satisfied for all spin pairs [1, 2, 11, 62, 63]. Examples of frustrated-spin quantum magnetism are quantum spin-ice, where the spins are highly correlated but fluctuate strongly before becoming ordered at low temperatures, and fluid-like quantum spin-liquids in which the fluctuating correlated spins persist down to zero temperature [1, 2, 62], as found in real materials like rare-earth pyrochlores [60, 61].

References

[1] Sachdev S 1999 *Quantum Phase Transitions* (Cambridge: Cambridge University Press)
[2] Lewenstein M, Sanpera A, Ahufinger V, Damski B, Sen A and Sen U 2007 *Adv. Phys.* **56** 243
[3] Bloch I, Dalibard J and Zwerger W 2008 *Rev. Mod. Phys.* **80** 885
[4] Jaksch D and Zoller P 2005 *Ann. Phys., NY* **315** 52
[5] Simon J, Bakr W S, Ma R, Tai M E, Preiss P M and Greiner M 2011 *Nature* **472** 307
[6] Hart R A, Duarte P M, Yang T-L, Liu X, Paiva T, Khatami E, Scalettar R T, Trivedi N, Huse D A and Hulet R G 2015 *Nature* **519** 211
[7] Zeiher J, van Bijnen R, Schauß P, Hild S, Choi J-Y, Pohl T, Bloch I and Gross C 2016 *Nat. Phys.* **12** 1095–9
[8] Labuhn H, Barredo D, Ravets S, de Léséleuc S, Macrí T, Lahaye T and Browaeys A 2016 *Nature* **534** 667
[9] Medley P, Weld D M, Miyake H, Pritchard D E and Ketterle W 2011 *Phys. Rev. Lett.* **106** 195301
[10] Büchler H P, Demler E, Lukin M, Micheli A, Prokofév N, Pupillo G and Zoller P 2007 *Phys. Rev. Lett.* **98** 060404
[11] Glaetzle A W, Dalmonte M, Nath R, Gross C, Bloch I and Zoller P 2015 *Phys. Rev. Lett.* **114** 173002
[12] Ghanbari S, Kieu T D, Sidorov A and Hannaford P 2006 *J. Phys. B: At. Mol. Opt. Phys.* **39** 847
[13] Singh M, Volk M, Akulshin A, Sidorov A, McLean R and Hannaford P 2008 *J. Phys. B: At. Mol. Opt. Phys.* **41** 065301
[14] Whitlock S, Gerritsma R, Fernholz T and Spreeuw R J C 2009 *New J. Phys.* **11** 023021
[15] Schmied R, Leibfried D, Spreeuw R J C and Whitlock S 2010 *New J. Phys.* **12** 103029
[16] Jose S, Surendran P, Wang Y, Herrera I, Krzemien L, Whitlock S, McLean R, Sidorov A and Hannaford P 2014 *Phys. Rev.* A **89** 051602(R)
[17] Surendran P, Jose S, Wang Y, Herrera I, Hu H, Liu X, Whitlock S, McLean R, Sidorov A and Hannaford P 2015 *Phys. Rev.* A **91** 023605
[18] Herrera I *et al* 2015 *J. Phys. D: Appl. Phys.* **48** 115002
[19] Müller M, Lesanovsky I, Weimer H, Büchler H P and Zoller P 2009 *Phys. Rev. Lett.* **102** 170502
[20] Weimer H, Müller M, Büchler H P and Lesanovsky I 2011 *Quantum Inf. Process.* **10** 885
[21] Nyman R A, Scheel S and Hinds E A 2011 *Quantum Inf. Process.* **10** 941
[22] Leung V Y F, Tauschinsky A, van Druten N J and Spreeuw R J C 2011 *Quantum Inf. Process.* **10** 955
[23] Saffman M, Walker T G and Mølmer K 2010 *Rev. Mod. Phys.* **82** 2313
[24] Beterov I I, Ryabtsev I I, Tretyakov D B and Entin V M 2009 *Phys. Rev.* A **79** 052504
[25] Leung V Y F *et al* 2014 *Rev. Sci. Instrum.* **85** 053102
[26] Robert-de Saint-Vincent M, Hofmann C S, Schempp H, Günter G, Whitlock S and Weidemüller M 2013 *Phys. Rev. Lett.* **110** 045004
[27] Schempp H *et al* 2014 *Phys. Rev. Lett.* **112** 013002

[28] Simonelli C, Valado M M, Masella G, Asteria L, Arimondo E, Ciampini D and Morsch O 2016 *J. Phys. B: At. Mol. Phys.* **49** 154002
[29] Ebert M, Gill A, Gibbons M, Zhang X, Saffman M and Walker T G 2014 *Phys. Rev. Lett.* **112** 043602
[30] Schlagmüller M *et al* 2016 *Phys. Rev. Lett.* **116** 053001
[31] Böttcher F, Gaj A, Westphal K M, Schlagmüller M, Kleinbach K S, Löw R, Liebisch T C, Pfau T and Hofferberth S 2016 *Phys. Rev.* A **93** 032512
[32] Kostelecký V A and Nieto M M 1985 *Phys. Rev.* A **32** 3243
[33] Fung Y H, Sompet P and Andersen M F 2016 *Technologies* **4** 4
[34] Beterov I I *et al* 2013 *Phys. Rev.* A **88** 010303(R)
[35] van Bijnen R M W 2011 Quantum engineering with ultracold atoms *PhD Thesis* Technische Universiteit Eindhoven
[36] Kenzelmann M, Coldea R, Tennant D A, Visser D, Hofmann M, Smeibidl P and Tylczynski Z 2002 *Phys. Rev.* B **65** 144432
[37] Breunig O, Garst M, Sela E, Buldmann B, Becker P, Bohatý L, Müller R and Lorenz T 2013 *Phys. Rev. Lett.* **111** 187202
[38] Lacroix C, Mendels P and Mila F 2011 *Introduction to Frustrated Magnetism: Materials, Experiments, Theory* (*Springer Series in Solid-State Sciences*) (Berlin: Springer)
[39] Yang C N and Yang C P 1966 *Phys. Rev.* **150** 321
[40] Melko R G, Paramekanti A, Burkov A A, Vishwanath A, Sheng D N and Balents L 2005 *Phys. Rev. Lett.* **95** 127207
[41] Melko R G 2007 *J. Phys.: Condens. Matter* **19** 145203
[42] Isakov S V, Wessel S, Melko R G, Sengupta K and Kim Y B 2006 *Phys. Rev. Lett.* **97** 147202
[43] Damle K and Senthil T 2006 *Phys. Rev. Lett.* **97** 067202
[44] Nath R, Dalmonte M, Glaetzle A W, Zoller P, Schmidt-Kaler F and Gerritsma R 2015 *New J. Phys.* **17** 065018
[45] Melko R G, del Maestro A and Burkov A A 2006 *Phys. Rev.* B **74** 214517
[46] Dmitriev D V and Krivnov V Y 2004 *Phys. Rev.* B **70** 144414
[47] Toskovic R, van den Berg R, Spinelli A, Eliens I S, van den Toorn B, Bryant B, Caux J-S and Otte A F 2016 *Nat. Phys.* **12** 656–60
[48] Dutta A, Aeppli G, Chakrabarti B K, Divakaran U, Rosenbaum T F and Sen D 2010 *Quantum Phase Transitions in Transverse Field Spin Models: From Statistical Physics to Quantum Information* (Cambridge: Cambridge University Press)
[49] Nussinov Z and van den Brink J 2015 *Rev. Mod. Phys.* **87** 1
[50] Marcuzzi M, Minář J, Barredo D, de Léséleuc S, Labuhn H, Lahaye T, Browaeys A, Levi E and Lesanovsky I 2017 *Phys. Rev. Lett.* **118** 063606
[51] Günter G, Robert-de Saint-Vincent M, Schempp H, Hofmann C S, Whitlock S and Weidemüller M 2012 *Phys. Rev. Lett.* **108** 013002
[52] Günter G, Schempp H, Robert-de Saint-Vincent M, Gavryusev V, Helmrich S, Hofmann C S, Whitlock S and Weidemüller M 2013 *Science* **342** 954
[53] Freeman R R and Economou N P 1979 *Phys. Rev.* A **20** 2356
[54] Endres M *et al* 2011 *Science* **334** 200
[55] McGuirk J M, Harber D M, Obrecht J M and Cornell E A 2004 *Phys. Rev.* A **69** 062905
[56] Tauschinsky A, Thijssen R M T, Whitlock S, van Linden van den Heuvell H B and Spreeuw R J C 2010 *Phys. Rev.* A **81** 063411
[57] Hermann-Avigliano C, Teixeira R C, Nguyen T L, Cantat-Moltrecht T, Nogues G, Dotsenko I, Gleyzes S, Raimond J M, Haroche S and Brune M 2014 *Phys. Rev.* A **90** 040502
[58] Sedlacek J A, Kim E, Rittenhouse S T, Weck P F, Sadeghpour H R and Shaffer J P 2016 *Phys. Rev. Lett.* **116** 133201
[59] Vermersch B, Glaetzle A W and Zoller P 2015 *Phys. Rev.* A **91** 023411
[60] Savary L and Balents L 2012 *Phys. Rev. Lett.* **108** 037202
[61] Savary L and Balents L 2013 *Phys. Rev.* B **87** 205130
[62] Balents L 2010 *Nature* **464** 199
[63] Glaetzle A W, Dalmonte M, Nath R, Rousochatzakis I, Moessner R and Zoller P 2014 *Phys. Rev.* X **4** 041037